Potential Energy Curves and Binding Energies of Heteronuclear Ultralong-Range Rydberg Molecules: Case Study of the Rb-Cs system

Qing Li[1,2], Shi-Yao Shao[1,2], Li-Hua Zhang[1,2], Bang Liu[1,2], Zheng-Yuan Zhang[1,2], Jun Zhang[1,2], Qi-Feng Wang[1,2], Han-Chao Chen[1,2], Yu Ma[1,2], Tian-Yu Han[1,2], Dong-Sheng Ding[1,2,*], and Bao-Sen Shi[1,2]
[1] *Laboratory of Quantum Information, University of Science and Technology of China, Hefei, Anhui 230026, China. and*
[2] *Synergetic Innovation Center of Quantum Information and Quantum Physics, University of Science and Technology of China, Hefei, Anhui 230026, China.*
(Dated: September 9, 2026)

Ultralong-range Rydberg molecules (ULRMs) have attracted significant interest due to their unique formation mechanisms and distinctive properties. We theoretically investigate the formation and characteristics of heteronuclear ULRMs, focusing on Rb-Cs systems. We calculate the vibrational energy levels of nS heteronuclear ULRMs and extend our analysis to polyatomic systems, tracing the evolution of binding energies as the molecular configuration changes. Our theoretical results are presented in terms of potential energy curves and the associated vibrational spectra, providing insight into the formation dynamics of these systems. These results also provide a framework for experimental efforts in probing heteronuclear ULRMs, which serve as a sensitive platform for investigating the fundamental properties of Rydberg atoms and their interactions with ground-state atoms, while providing a benchmark for *ab initio* calculations.

I. INTRODUCTION

Since the proposal by Greene et al. in 2000 [1], ultralong-range Rydberg molecules (ULRMs) have become a significant focus of research in quantum and molecular physics. Unlike conventional molecules that are bound by covalent or ionic interactions, ULRMs are formed through a unique binding mechanism driven by the scattering interaction between Rydberg electrons and ground-state atoms. This distinctive binding mechanism allows ULRMs to achieve molecular sizes comparable to the Rydberg atoms that form them, typically on the order of 100 nm. Such large molecular sizes and the distinctive binding mechanism have sparked considerable interest in ULRMs, as they are expected to provide new insights into molecular behaviors and quantum effects, such as Stark effect of ULRMs [2], the formation of homonuclear molecules with permanent electric dipole moments [3] and the coupling of a single electron to a Bose–Einstein condensate [4].

A prominent example of ULRMs is the so-called "trilobite" molecule, formed when the presence of a ground-state atom causes the Rydberg electron to localize around it [1]. This localization leads to exceptionally large permanent electric dipole moments (PEDMs) reaching thousands of Debye [5], even in homonuclear ULRMs. In these molecules, significant PEDMs arise not from differences in atomic species, but rather from the asymmetric spatial distribution of the Rydberg electron wave function [3]. This asymmetry results from localized scattering interactions with the ground-state atoms and the specific geometric arrangement within the molecule.

The existence of these large PEDMs enables experimental studies into their interaction with external electromagnetic fields. The PEDMs of Rb(nS) and Cs(nS) ULRMs [3, 5] were probed via electric-field-induced spectral line broadening, while Rb(nF) trilobite Rydberg molecules were directly prepared by three-photon excitation, with their PEDMs characterized using the same method [6]. Pendular butterfly Rydberg molecules were also observed under applied electric fields [7]. Recent advancements also show that the spatial orientation of these molecules is manipulated via external fields, enabling precise control of their alignment, including via weak magnetic fields exploiting the angular structure of D-state Rydberg orbitals [8], and spin–orbit coupling combined with weak magnetic fields even in S-state molecules [9].

In addition, polyatomic ULRMs have been proposed and actively investigated in recent years. One particularly intriguing class consists of a Rydberg atom bound to a polar molecule, where the long-range charge–dipole interaction plays a central role in the molecular binding [10, 11]. The rotational hybridization of the polar molecule in such systems, as well as the control of molecular alignment and orientation, have also been theoretically explored [12]. In addition, experimental protocols for the realization of these polyatomic Rydberg molecules have been proposed [13]. Recently, the observation of Rydberg blockade induced by the charge–dipole interaction between an atom and a polar molecule has been demonstrated using optical tweezers, establishing a promising platform for the photoassociation of such hybrid polyatomic Rydberg molecules [14]. Another important class of polyatomic ULRMs consists of a single Rydberg atom binding multiple ground-state atoms via low-energy electron scattering, which has been successfully demonstrated experimentally. For isotropic nS Rydberg states,

* Corresponding author: dds@ustc.edu.cn

the binding energies scale as nearly integer multiples of the dimer energy, reflecting the negligible interactions among the captured ground-state atoms [15]. In contrast, the strong anisotropy of nD states leads to the formation of angular trimers with pronounced non-additive binding energies [16]. Furthermore, in the high-density regime, perturbation-induced quantum scarring can promote the formation of polyatomic trilobite molecules governed by specific geometric constraints [17, 18].

The lifetimes of ULRMs have been systematically studied both experimentally and theoretically. Experiments show that Rb_2 ULRMs have significantly shorter lifetimes than the corresponding Rydberg atoms [2]. Their decay rates increase linearly with ground-state atom density due to collisional loss, and vibrationally excited states are even less stable because of quantum reflection and inward-penetration loss channels [19, 20]. In contrast, Sr_2 ULRMs exhibit lifetimes comparable to those of the corresponding Rydberg atoms, owing to the absence of a low-energy p-wave shape resonance in electron–Sr scattering [21]. However, at sufficiently high atomic densities, the lifetimes of Sr_2 ULRMs are also significantly reduced [22].

The study of heteronuclear ULRMs, which offers a broader range of tunable molecular properties compared to homonuclear ULRMs, has recently gained significant attention. These properties include large dipole moments, varied binding energies, and more complex interactions with external fields. Such flexibility makes heteronuclear ULRMs an exciting area for both theoretical research and experimental exploration, including theoretical studies on various alkali-metal combinations [23], Hg*Rb heteronuclear ULRMs [24], isotope-heteronuclear ULRMs in Sr [25], Cs*K heteronuclear ULRMs [26], and Rb*Cs molecules based on optical tweezer techniques [27]. Unlike homonuclear systems, heteronuclear systems provide a unique opportunity to manipulate atomic composition, allowing for more precise control over molecular characteristics and behavior. This ability to fine-tune molecular properties is especially valuable for applications in the study of pair-correlation functions in atomic mixtures [28, 29] and the creation of ultracold ion-pair systems with variable mass ratio [30].

In this paper, we focus on investigating the formation and properties of diatomic and polyatomic heteronuclear ULRMs. By calculating potential energy curves (PECs) and vibrational energy levels, we aim to gain insights into the behavior and interactions of diatomic heteronuclear ULRMs. In addition, this work presents the theoretical exploration of polyatomic heteronuclear ULRMs formation in high-density Cs and Rb cold atomic gases. We also provide the calculation of their expected experimental vibrational spectra. The advantage of polyatomic heteronuclear ULRMs is their increased complexity, which provides a richer platform for investigating multi-body interactions and the emergence of novel quantum phenomena in strongly correlated systems.

II. CALCULATION

A. Hamiltonian for Diatomic ULRMs

ULRMs consist of a Rydberg atom and one or more ground-state atoms, where the ground-state atom is bound to the electron orbit due to low-energy scattering interactions with the electron [1], as shown in Fig. 1. All calculations throughout this paper are performed in atomic units.

We begin by considering the case of a single ground-state atom, i.e., diatomic ULRMs. Under the Born–Oppenheimer approximation, we take the atomic nucleus as the origin of coordinates. The coordinate of the Rydberg electron is denoted by $\vec{r}$ and the ground-state atom's coordinate denoted as $\vec{R}$, The molecular Hamiltonian is then expressed as:

$$H = H_0(\vec{r}) + V_{ea}(\vec{R} - \vec{r}) + V_{ca}(\vec{R}) + H_{HF} + H_{vib} + H_{rot}, \quad (1)$$

here, $H_0(\vec{r})$, $V_{ea}(\vec{R}-\vec{r})$, $V_{ca}(\vec{R})$, $H_{\rm HF}$, $H_{\rm vib}$, and $H_{\rm rot}$ denote the Hamiltonian of the isolated Rydberg atom, the electron–atom scattering interaction, the ionic core–atom interaction, the hyperfine interaction of the ground-state atom, the molecular vibrational energy, and the molecular rotational energy, respectively. The interaction $V_{ca}(\vec{R})$ between the ionic core and the ground-state atom is neglected in the relatively high principal quantum number regime considered in this work, as it takes the form $V_{ca}(\vec{R}) = -\alpha/2R^4$, where α is the polarizability of the ground-state atom. This interaction decays rapidly with distance and thus contributes negligibly to the molecular potential at the large internuclear separations relevant to ULRMs.

The hyperfine structure of the Rydberg atom is also neglected, as the Rydberg electron is far from the nucleus, making this contribution extremely weak. The rotational energy is neglected because the large molecular size leads to a large moment of inertia, yielding rotational level spacings too small to be spectroscopically resolved. Therefore, the total Hamiltonian of ULRMs is simplified to:

$$H = H_0(\vec{r}) + V_{ea}(\vec{R} - \vec{r}) + H_{HF} + H_{vib}, \quad (2)$$

here, the eigenenergies of the first three terms, as functions of $\left|\vec{R}\right|$, represent the potential energy curves (PECs) under the Born–Oppenheimer approximation. Figure 1 illustrates the structure of ULRMs and the angular momenta associated with these three types of interactions. The final term represents the vibrational energy of ULRMs, which is directly linked to their vibrational spectra, i.e., the most direct method currently available for observing these molecules.

In Eq. (2), $H_0(\vec{r})$ includes the kinetic and potential energy of the Rydberg electron in the ionic core field. The eigenenergies of alkali-metal Rydberg states are

$$E_{nlj} = -\frac{1}{2(n-\delta_{nlj})^2}, \quad (3)$$

where n, l, and j are the principal, orbital, and total angular momentum quantum numbers, respectively, and δ_{nlj} is the quantum defect [31].

The hyperfine interaction of the ground-state atom is

$$H_{\mathrm{HF}} = A, \vec{I} \cdot \vec{s} * 2, \tag{4}$$

where I is the nuclear spin and $s_2 = 1/2$ is the electron spin. The corresponding hyperfine energies are

$$E * \mathrm{HF} = \frac{A}{2}\left[F(F+1) - I(I+1) - s_2(s_2+1)\right], \tag{5}$$

with $F = |\vec{I} + \vec{s}_2|$. For ^{87}Rb and ^{133}Cs, $I = 3/2$ and $7/2$, respectively, and the hyperfine constants are $A = 3417$ MHz and 2298 MHz, respectively.

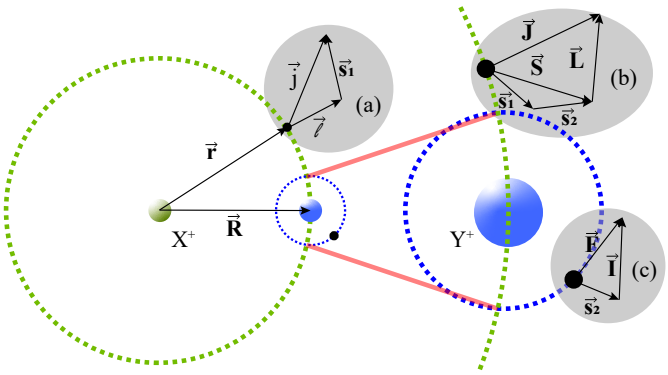


Figure 1. Schematic illustration of the angular momentum in ULRMs. The green, blue, and black spheres represent the atomic core of the Rydberg atom, the atomic core of the ground-state atom, and electrons, respectively. The green and blue dashed lines indicate the orbitals of the Rydberg and ground-state electrons. The right panel provides an magnified view of the local region near the ground-state atom. (a) Interaction within an isolated Rydberg atom, involving the orbital angular momentum l, the Rydberg electron spin s_1, and their coupling into the total angular momentum j. (b) Scattering interaction between the Rydberg electron and the ground-state atom, characterized by the orbital angular momentum L of the Rydberg electron relative to the ground-state atom, the electron spins s_1 and s_2, the total spin S, and the total angular momentum J. (c) Hyperfine interaction of the ground-state atom, resulting from the coupling of the ground-state electron spin s_2 and the nuclear spin I to form the total angular momentum F.

For the second term $V_{ea}(\vec{R}-\vec{r})$, following the approach of Fermi [32] and Omont [33], this interaction is modeled using a zero-range pseudopotential, and the s-wave and p-wave representations are given by [1, 34]:

$$V_p = 2\pi a_s(k)\,\delta(\vec{r}-\vec{R}) + 6\pi a_p^3(k)\,\overleftarrow{\nabla}\delta(\vec{r}-\vec{R})\overrightarrow{\nabla}, \tag{6}$$

here, $a_L^{2L+1}(k)$ is the scattering length or scattering volume of ground-state atom for s-wave ($L = 0$) or p-wave ($L = 1$), which play a crucial role in determining the strength of the electron–atom interaction. These quantities are related to the scattering phase shifts $\delta_s(k)$ and $\delta_p(k)$ of a free electron with wave number k scattering off the ground-state atom (the Rydberg electron is viewed as a free electron in this context), via the relations:

$$a_s(k) = -\frac{\tan(\delta_s(k))}{k}, \quad a_p^3(k) = -\frac{\tan(\delta_p(k))}{k^3}, \tag{7}$$

the phase shifts $\delta_s(k)$ and $\delta_p(k)$ are typically obtained through theoretical calculations calibrated by experimental data [35–37]. Furthermore, the wavenumber k of the Rydberg electron is expressed in semiclassical form as

$$k(r) = \sqrt{2\left(E_{nlj} + \frac{1}{r}\right)}, \tag{8}$$

which follows from energy conservation [33]. The scattering phase shift is determined by the long-range polarization potential, which leads to the Wigner threshold behavior $\delta \propto k^2$ as $k \to 0$. In contrast, the Omont pseudopotential model assumes a short-range interaction, resulting in $\delta \propto k^3$. Consequently, the ratio k^2/k^3 that appears in the effective scattering volume diverges in the low-energy limit. To regularize this divergence, we introduce a cutoff parameter $k_{\min}$ in our numerical implementation [31]. Different cutoff values are typically chosen for s-wave and p-wave scattering, with the cutoff for p-wave scattering set smaller to reflect its stronger low-energy divergence. This regularization procedure is physically justified, as the limit $k \to 0$ corresponds to an infinitely extended electronic wave function. The introduction of $k_{\min}$ ensures numerical stability while maintaining the physical reliability of the results.

The scattering phase shifts discussed above are categorized into only the s-wave and p-wave components, corresponding to angular momentum values $L = 0$ and $L = 1$ of the Rydberg electron relative to the ground-state atom. However, these classifications neglect the total angular momentum J resulting from the coupling of L with the total electronic spin S. In practice, the scattering channels corresponding to different J values exhibit notable differences. Khuskivadze *et al.* first introduced J-dependent scattering phase shifts into the theoretical framework using a Green's function formalism [35]. Later, Eiles *et al.* proposed a more tractable method that enables efficient diagonalization. Upon performing the coupling and decoupling of the relevant angular momenta, and choosing the internuclear axis as the quantization axis, the Fermi pseudopotential takes the following form [38]:

$$V_p = \delta(\vec{R}-\vec{r}) \sum_{LSJ} \sum_{\Omega} \sum_{M_L, M_L'} \mathcal{A}(SLJ,k)\, C^{J\Omega}_{LM_L,S(\Omega-M_L)} \times C^{J\Omega}_{LM_L',S(\Omega-M_L')}\, \overleftarrow{\nabla}^{(L)}_{M_L} |S(\Omega-M_L)\rangle\, \overrightarrow{\nabla}^{(L)}_{M_L'} \langle S(\Omega-M_L')|\,, \tag{9}$$

here, Ω denotes the projection of the total angular momentum J onto the internuclear axis, and $\mathcal{A}(SLJ,k) = (2L+1)\,2\pi\, a(SLJ,k)$,

where $a(SLJ,k)$ denotes the energy-dependent scattering length (or scattering volume, depending on the partial wave). The coefficient $C^{J\Omega}_{LM_L,\,S(\Omega-M_L)}$ is the Clebsch–Gordan coefficient describing the angular momentum coupling, and $|S(\Omega-M_L)\rangle$ represents the spin state resulting from the coupling of the two electron spins. The summation is carried out over all physically allowed combinations of L, S, and J, each corresponding to a distinct scattering channel. For $L=0$, the relevant channels are $^1S_0$ and $^3S_0$; for $L=1$, they include the $^1P_1$ and $^3P_{0,1,2}$ channels. As noted earlier, higher partial waves are neglected due to the low-energy nature of the Rydberg electron scattering process.

B. Construction of the Hamiltonian Matrix

To obtain the PECs of ULRMs, a general procedure involves diagonalizing the molecular Hamiltonian at each internuclear distance R in a suitable basis. The resulting eigenvalues, treated as functions of R, define the PECs of the ULRMs. Within the framework of the Born–Oppenheimer approximation, the nuclear motion is treated separately from the electronic dynamics. Therefore, the vibrational kinetic energy of the two nuclei corresponding to the last term in Eq. 2 is neglected at this stage. With this simplification, the problem reduces to solving the electronic Hamiltonian for fixed R, which requires an appropriate choice of basis states. A natural and efficient basis consists of the direct product states $|nljm_j\rangle\otimes|m_{s_2},m_{i_2}\rangle$, where $|nljm_j\rangle$ are the eigenstates of the Rydberg atom including fine-structure effects, and $|m_{s_2},m_{i_2}\rangle$ are the eigenstates of the ground-state atom's electron and nuclear spins. Furthermore, since only partial waves with $L=0$ and $L=1$ are considered in the scattering process, the magnetic quantum number M_L takes values of 0 or ±1. Given that $M_L=m_l$, it is sufficient to include only the basis states with $m_l=0,\pm1$, i.e., those states in $|nljm_j\rangle$ with $|m_j|\le 3/2$. The Rydberg eigenstates $|nljm_j\rangle$ are expressed as two-component spinor wave functions of the form:

$$\Psi_{nljm_j}(\vec{r})=\sum_{m,m_s} C^{jm_j}_{lm_l,sm_s}\,R_{nlj}(r)\,Y_{lm_l}(\vec{r})\,|m_s\rangle\,, \quad (10)$$

where $C^{jm_j}_{lm_l,sm_s}$ are the Clebsch–Gordan coefficients that couple the orbital and spin angular momenta, $R_{nlj}(r)$ denotes the radial wave function, and $Y_{lm_l}(\vec{r})$ represents the spherical harmonic function. The radial wave functions of alkali-metal atoms are obtained using the ARC package [39]. The spin state $|m_s\rangle$ refers to the spin projection of the Rydberg electron. The state of the ground-state atom is represented by the product state $|m_{s_2},m_{i_2}\rangle$, where m_{s_2} and m_{i_2} are the projections of the electron spin and nuclear spin, respectively. Therefore, the product basis $|m_{s_2},m_{i_2}\rangle$ spans a Hilbert space of dimension 8 (16) for ^{87}Rb (^{133}Cs).

In Eq. (2), H_0 represents the Hamiltonian of the isolated Rydberg atom. It is diagonalized in the chosen basis states and is expressed as:

$$\begin{aligned}\langle\beta|H_0(\vec{r})|\alpha\rangle &= \langle n'l'j'm'_j|H_0(\vec{r})|nljm_j\rangle \\ &\quad\cdot\langle m'_{s_2}m'_{i_2}|m_{s_2}m_{i_2}\rangle=\delta_{\alpha\beta}E_{nlj},\end{aligned} \quad (11)$$

here, $|\alpha\rangle$ and $\langle\beta|$ are shorthand notations for the states $|nljm_j\rangle\otimes|m_{s_2}m_{i_2}\rangle$ and $\langle m'_{s_2}m'_{i_2}|\otimes\langle n'l'j'm'_j|$, respectively.

In Eq. (2), $H_{\rm HF}$ denotes the hyperfine interaction operator of the ground-state atom. Its eigenstates are the total spin states $|Fm_F\rangle$, hence it is not fully diagonal in the chosen basis. By using CG coefficients, the uncoupled basis states $|m_{s_2},m_{i_2}\rangle$ can first be expanded into coupled states, and then the matrix elements are calculated accordingly. This is expressed as:

$$\begin{aligned}\langle\beta|H_{HF}|\alpha\rangle &= \langle n'l'j'm'_j|nljm_j\rangle\cdot\langle m'_{s_2}m'_{i_2}|A\vec{I}\cdot\vec{s}_2|m_{s_2}m_{i_2}\rangle \\ &= \frac{A}{2}\delta_{(n'l'j'm_j)(nljm_j)}\sum_{FM_F} C^{FM_F}_{m_{s_2},m_{i_2}}C^{FM_F}_{m'_{s_2},m'_{i_2}} \\ &\quad\cdot\left[F(F+1)-I(I+1)-s_2(s_2+1)\right].\end{aligned} \quad (12)$$

In Eq. (2), $V_{ea}(\vec{R})$ is represented by the Fermi pseudopotential V_p, whose explicit form is given in Eq. (9). The matrix elements of V_p can therefore be written as:

$$\begin{aligned}\langle\beta|V_P|\alpha\rangle =& \delta(\vec{R}-\vec{r})\sum_{LSJ}\sum_{\Omega}\sum_{M_L,M'_L}A(SLJ,k) \\ &\times C^{J\Omega}_{LM_L,\,S(\Omega-M_L)}C^{J\Omega}_{LM'_L,\,S(\Omega-M'_L)} \\ &\times\left\langle\beta\left|\overleftarrow{\bar{\nabla}}^{(L)}_{M_L}\right|S(\Omega-M_L)\right\rangle\left\langle S(\Omega-M'_L)\left|\overrightarrow{\bar{\nabla}}^{(L)}_{M'_L}\right|\alpha\right\rangle.\end{aligned} \quad (13)$$

Following the method of Eiles *et al.*, we introduce the symbol Q to denote which is defined as [38]:

$$\begin{aligned}Q^{nlj}_{LM_L}(R) &= \delta_{m,M_L}\left[\vec{\nabla}^{\,L}\left(\phi_{nljm}(\vec{R})\right)\right]^{L}_{M_L}, \\ \text{where}\quad Q^{nlj}_{00}(R) &= R_{nlj}(R)\sqrt{\frac{2l+1}{4\pi}}, \\ Q^{nlj}_{10}(R) &= \sqrt{\frac{2l+1}{4\pi}}\,\partial_R R_{nlj}(R), \\ Q^{nlj}_{\pm1}(R) &= \frac{R_{nlj}(R)}{R}\sqrt{\frac{(2l+1)(l+1)l}{8\pi}}, \qquad l>0.\end{aligned} \quad (14)$$

here, $\phi_{nljm}(\vec{R})=R_{nlj}(r)\,Y_{lm}(\vec{r})$. Next, by substituting the full forms of $|\alpha\rangle$ and $\langle\beta|$ into Eq. (13), we obtain:

$$\begin{aligned}\left\langle S(\Omega-M'_L)\left|\bar{\nabla}^{(L)}_{M'_L}\right|\alpha\right\rangle &= \sum_{m_{s_1}}\delta_{M'_L(m_j-m_{s_1})}\,C^{jm_j}_{l(m_j-m_{s_1}),\,s_1m_{s_1}} \\ &\quad\times Q^{nlj}_{LM'_L}\,\langle S(\Omega-M'_L)|m_{s_1}m_{s_2}\rangle|m_{i_2}\rangle\,,\end{aligned} \quad (15)$$

$$\begin{aligned}\left\langle\beta\left|\bar{\nabla}^{(L)}_{M_L}\right|S(\Omega-M_L)\right\rangle &= \sum_{m'_{s_1}}\delta_{M_L(m'_j-m'_{s_1})}\,C^{j'm'_j}_{l'(m'_j-m'_{s_1}),\,s'_1m'_{s_1}} \\ &\quad\times Q^{n'l'j'}_{LM_L}\,\langle m'_{s_1}m'_{s_2}|S(\Omega-M_L)\rangle\,\langle m_{i'_2}|\,.\end{aligned} \quad (16)$$

By substituting Eq. 15 and Eq. 16 into Eq. 13, we obtain the complete matrix elements of the Fermi pseudopotential. Finally, by adding Eq. 11, Eq. 12, and Eq. 13, we obtain the full Hamiltonian matrix.

However, a rough estimation reveals that when the principal quantum number n is around 30, the number of basis states can reach up to 10^4. This leads to a large matrix, and diagonalization at each internuclear distance R makes cost reduction essential. An important consideration is that the total magnetic quantum number, $\Omega = m_j + m_{s_2} + m_{i_2}$, is a good quantum number of the system. As a result, the Hamiltonian matrix has a block-diagonal structure, where each block corresponds to a fixed value of Ω. This implies that the matrix elements satisfy $\langle\alpha|H|\beta\rangle \propto \delta_{\Omega_\alpha\Omega_\beta}$, and thus the full diagonalization is reduced to the diagonalization of smaller submatrices. Consequently, the computational cost is significantly reduced by diagonalizing each block independently.

C. Vibrational Energy Levels of Diatomic ULRMs

By diagonalizing the matrix constructed above, we can obtain the PECs of the ULRMs. However, the atomic nuclei are not stationary; instead, they undergo vibrational motion within these PECs. This motion is described by the fourth term in Eq. (2), which corresponds to the nuclear vibrational energy. The vibrational energy levels and wave functions are calculated within the framework of the Born–Oppenheimer approximation. In the center-of-mass frame of the Rydberg and ground-state atoms, the vibrational dynamics of the ULRMs are modeled as the motion of a single particle with reduced mass $\mu = m_1 m_2/(m_1 + m_2)$, where m_1 and m_2 denote the masses of the Rydberg and ground-state atoms, respectively. The quantum dynamics of this effective particle moving in the PEC is governed by the Schrödinger equation [40]:

$$\left[-\frac{\nabla_R^2}{2\mu} + U(R)\right]\chi_v(R) = E_v\chi_v(R), \tag{17}$$

where $U(R)$ represents the calculated PECs, and E_v and $\chi_v(R)$ denote the vibrational energy and wave function associated with vibrational quantum number v, respectively. The electron mass is set to 1, and the masses of ^{87}Rb and ^{133}Cs are taken to be 158432 and 242282, respectively. The vibrational Schrödinger equation is solved numerically using the finite difference method (FDM), which discretizes the coordinate space into a grid and approximates the derivatives using finite differences. This approach transforms the differential equation into a matrix eigenvalue problem, enabling efficient and accurate computation of vibrational energy levels and corresponding nuclear wave functions. The resulting vibrational spectra and wave functions are illustrated in Fig. 2.

D. Theoretical Extension to Polyatomic ULRMs

While initial research focused on diatomic ULRMs, Gaj *et al.* demonstrated the formation of polyatomic molecules where an nS Rydberg atom simultaneously captures multiple ground-state atoms [15]. Their work confirmed that, due to the isotropy of the nS Rydberg wavefunction and the negligible interactions among the captured ground-state atoms, the binding energies are additive. Building on this independent perturber approximation, we extend the theoretical framework to predict the spectra of polyatomic heteronuclear ULRMs in ultracold Rb and Cs mixtures. Our calculation targets the vibrational ground states within the outermost deep potential wells of the molecular PECs, as these states typically possess the largest Franck-Condon factors. We define $\epsilon_{\mathrm{Rb}}(\epsilon_{\mathrm{Cs}})$ as the fundamental binding energies of a single ground-state Rb(Cs) atom bound to a specific central Rydberg core, respectively. Consequently, for a polyatomic ULRM consisting of a central Rydberg atom, n_{Rb} ground-state Rb atoms, and n_{Cs} ground-state Cs atoms, the total spectral shift $\Delta E(n_{\mathrm{Rb}}, n_{\mathrm{Cs}})$ relative to the atomic Rydberg line is given by:

$$\Delta E(n_{\mathrm{Rb}}, n_{\mathrm{Cs}}) = n_{\mathrm{Rb}} \cdot \epsilon_{\mathrm{Rb}} + n_{\mathrm{Cs}} \cdot \epsilon_{\mathrm{Cs}}. \tag{18}$$

By applying this additivity rule to both Rb and Cs centered Rydberg systems, we systematically calculate the energy levels for various polyatomic configurations, establishing a theoretical framework to interpret the spectral features presented in the following sections.

III. RESULT

A. Diatomic heteronuclear ULRMs

As shown in Eq. (9), the scattering length of the ground-state atom plays a pivotal role in determining the bond strength of molecules, while the properties of the Rydberg atom govern the energy level structure of these molecules. Consequently, when ULRMs are formed by two different atomic species, heteronuclear ULRMs can exhibit a broader range of physical properties. As discussed in Sec. I, heteronuclear ULRMs have been extensively studied both experimentally and theoretically. However, a detailed comparison of the vibrational energy levels in the outermost potential wells between homonuclear and heteronuclear ULRMs is still lacking.

The PECs for the $37S$ Rydberg state, along with the corresponding vibrational energy levels and wave functions of heteronuclear Rydberg molecules, are shown in Fig. 2. Figure 2 shows that, regardless of the atomic species involved, all PECs feature both shallow and deep potential wells. This structure arises from the singlet-triplet character induced by spin coupling between the Rydberg and ground-state electrons. The shallow wells correspond to singlet-triplet mixed states (total spin $S =$

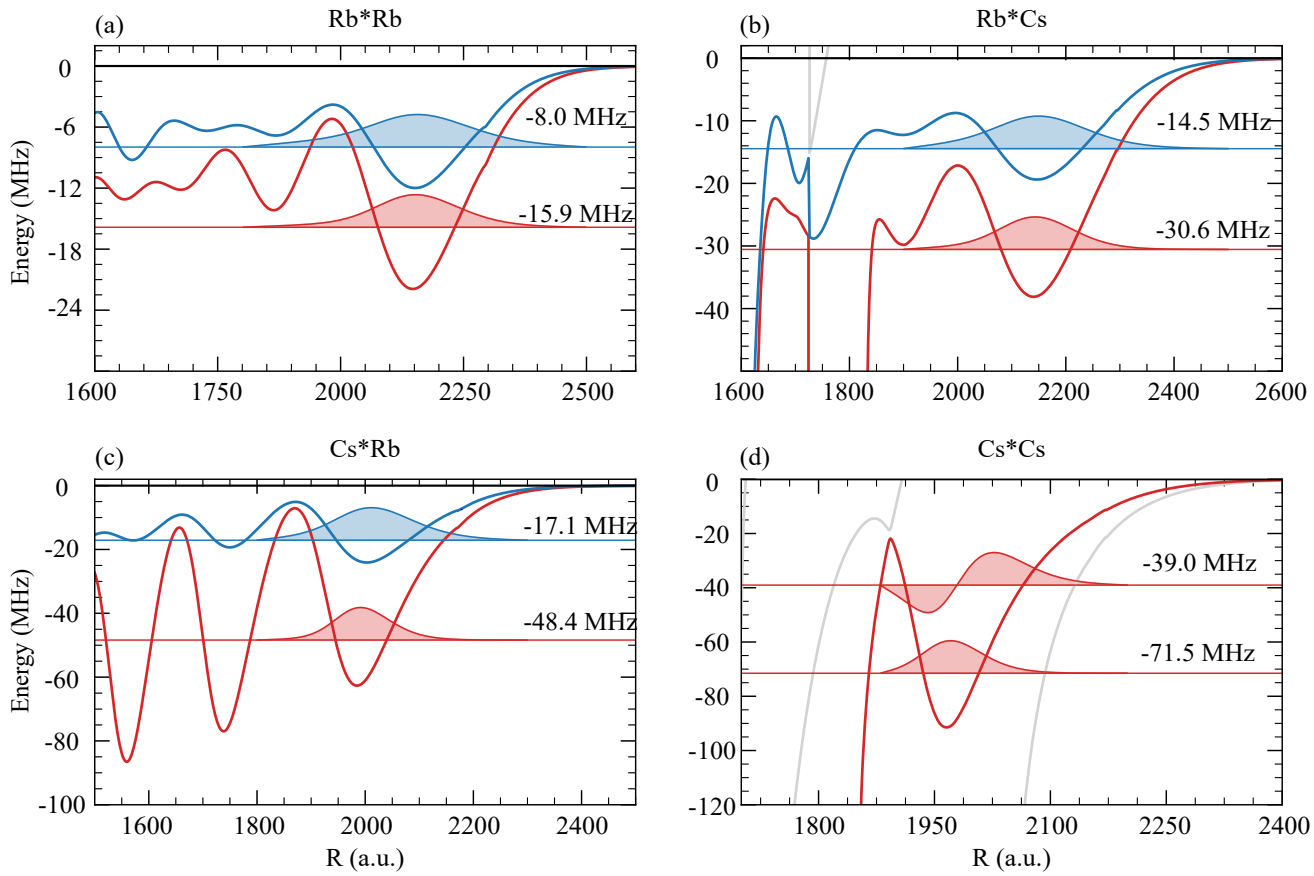


Figure 2. Vibrational energy levels and wave functions in the outermost potential wells of $(37S_{1/2}, F = 1 \text{ or } 3, \Omega = 0.5)$ ULRMs. (a)–(d) Outermost potential wells for Rb*Rb, Rb*Cs, Cs*Rb, and Cs*Cs ULRMs, respectively, where the asterisk (*) denotes the Rydberg atom. In contrast to panels (a)–(c), where only the ground vibrational state ($v = 0$) is shown for each potential well, panel (d) explicitly illustrates two vibrational states, $v = 0$ and $v = 1$, supported by the potential well. All potential energy curves are plotted relative to the asymptotic atomic energy levels of the corresponding $(37S_{1/2}, F = 1$ for Rb or $F = 3$ for Cs) state, where the hyperfine quantum number F corresponds to the ground-state atom. Horizontal thin lines indicate the vibrational energy levels, with the corresponding vibrational wave functions shown as identically colored curves. The outermost molecular potential wells split into two components due to hyperfine interactions: a deep well primarily associated with the spin-triplet state and a shallow well arising from a singlet–triplet mixed state. (Note: The deep well for Cs*Cs is not shown.)

0 and $S = 1$), while the deep wells are associated with the triplet state ($S = 1$) [38, 41]. Moreover, when the Cs atom acts as the Rydberg atom, the large quantum defect $\delta_s = 4.05$ [42] for the S-state leads to a near-degeneracy between the nS state and the $(n-4)l$ states with $l > 2$. This near-degeneracy results in strong coupling, which significantly deepens the outermost potential wells compared to those associated with Rb Rydberg atoms. Finally, when Cs serves as the ground-state atom, both the shallow and deep potential wells are further deepened, indicating stronger interactions in heteronuclear configurations involving Cs. The increased well depths allow for the formation of a greater number of bound vibrational states.

The vibrational ground-state energy levels of the four types of ULRMs, as functions of the principal quantum number n, are shown in Fig. 3. It is evident that, for all values of n, replacing the ground-state atom from Rb to Cs consistently leads to lower vibrational energy levels, indicating a stronger binding interaction. To elucidate the effect of replacing the Rydberg atom from Rb to Cs, we further analyze the power-law dependence of these vibrational levels on the effective principal quantum number $n^* = n - \delta$, using the fitting relation $|E_b| = a(n^*)^b$. For the shallow potential wells, the fitted exponents are $b = -6.82$ for Rb*Rb and $b = -7.80$ for Cs*Rb molecules, indicating that the vibrational levels of Cs*Rb change more rapidly with increasing n than those of Rb*Rb. As a result, although the vibrational levels of Cs*Rb are lower at small n, they gradually approach those of Rb*Rb at larger n. This trend can be attributed to the evolution of the Cs atomic energy structure with increasing n, which weakens the coupling strength between the Cs S state and high-l states, thereby significantly influencing

the potential well depth and the resulting vibrational levels. Similar trends are also observed in the deep potential wells, with fitted exponents of $b = -6.41$ for Rb*Rb and $b = -8.28$ for Cs*Rb. These results demonstrate that the choice of Rydberg and ground-state atomic species systematically governs the vibrational properties of the molecules, representing a universal feature of such ULRMs.

From an experimental perspective, we predict that in an ultracold two-species atomic gas composed of Rb and Cs, all four types of heteronuclear ULRMs are formed simultaneously if the Rb and Cs atoms are independently excited to their respective Rydberg states using two distinct lasers, with the excitation frequencies scanned near resonance.

B. Polyatomic heteronuclear ULRMs

Based on the calculations presented in Fig. 2, we analyze the spectral characteristics of polyatomic heteronuclear ULRMs by applying the additivity rule defined in Eq. (18). For the $37S_{1/2}$ Rydberg state, the fundamental binding energies in the outermost deep potential wells are determined as $\epsilon_{\rm Rb}(\epsilon_{\rm Cs}) = -15.9(-30.6)$ MHz for the Rb-centered system, while for the Cs-centered system, they are $\epsilon_{\rm Rb}(\epsilon_{\rm Cs}) = -48.4(-71.5)$ MHz. By utilizing these dimer energies, we obtain the polyatomic energy levels illustrated in Fig. 4. As the formation of polyatomic molecules requires high-density atomic clouds to capture multiple ground-state atoms, our analysis focuses on configurations where the total number of ground-state atoms $n_{\rm Rb} + n_{\rm Cs} \leq 4$.

In Fig. 4, the atomic configurations $(n_{\rm Rb}, n_{\rm Cs})$ are labeled alongside each spectral line. A significant feature of these heteronuclear spectra is the emergence of near-degeneracy among different configurations. In the Rb-centered system (upper panel), the binding energy of a ground-state Cs atom is approximately twice that of a ground-state Rb atom ($\epsilon_{\rm Cs} \approx 2\epsilon_{\rm Rb}$). Consequently, replacing one Cs atom with two Rb atoms results in nearly identical total energy shifts, leading to quasi-degenerate configurations such as $(n_{\rm Rb} = 3, n_{\rm Cs} = 0)$ and $(1, 1)$. Other degenerate clusters include $(0, 2)$, $(2, 1)$, and $(4, 0)$, among others. For the Cs-centered system (bottom panel), a different ratio of $2\epsilon_{\rm Cs} \approx 3\epsilon_{\rm Rb}$ is observed at $n = 37$, making configurations such as $(n_{\rm Rb} = 3, n_{\rm Cs} = 0)$ and $(0, 2)$ nearly degenerate.

These degeneracy patterns are sensitive to the principal quantum number n. For the $38S_{1/2}$ state, the calculated fundamental binding energies shift to $\epsilon_{\rm Rb} = -13.2$ MHz and $\epsilon_{\rm Cs} = -25.3$ MHz for the Rb core, and $\epsilon_{\rm Rb} = -37.8$ MHz and $\epsilon_{\rm Cs} = -46.8$ MHz for the Cs core. While the relationship $\epsilon_{\rm Cs} \approx 2\epsilon_{\rm Rb}$ remains approximately valid for the Rb-centered system at $n = 38$, the $2\epsilon_{\rm Cs} \approx 3\epsilon_{\rm Rb}$ condition for the Cs-centered system no longer holds. This demonstrates that the specific degeneracy behavior observed at $n = 37$ depends on the n-scaling of the interactions and is not a universal feature across all Rydberg states.

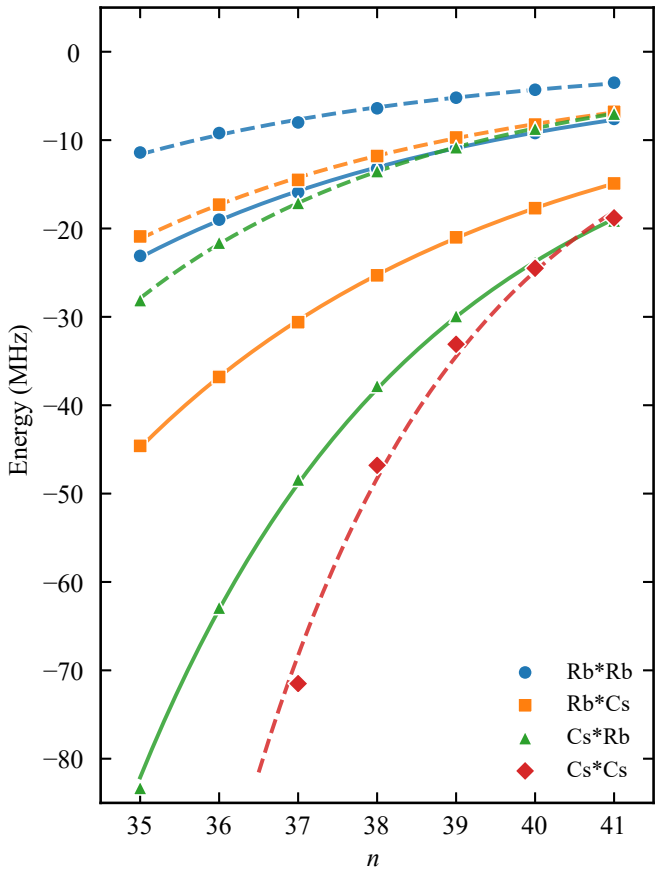


Figure 3. Vibrational ground-state energies of the outermost potential wells for four types of ULRMs ($\Omega = 0.5$), including both shallow (dashed curves) and deep (solid curves) potential wells. Circles, squares, triangles, and diamonds represent Rb*Rb, Rb*Cs, Cs*Rb, and Cs*Cs molecules, respectively. The data spans principal quantum numbers from $n = 35$ to $n = 41$. Cs*Cs molecules are not shown for $n = 35$ and 36 due to their extremely deep potential wells, arising from an almost integer-valued quantum defect ($\delta = 4.05$). Curves depict power-law fits $|E_b| \propto (n^*)^b$ with $n^* = n - \delta$. The fitted exponents b for shallow wells are -6.82 (Rb*Rb), -6.53 (Rb*Cs), -7.80 (Cs*Rb), and -11.60 (Cs*Cs, $n \geq 37$). For deep wells, $b = -6.41$ (Rb*Rb), -6.37 (Rb*Cs), and -8.28 (Cs*Rb).

As the number of ground-state atoms increases, the vibrational spectra become increasingly congested, with several polyatomic species appearing within a window of only a few MHz. While these configurations are theoretically distinct, their experimental resolution requires careful consideration of laser linewidths and molecular identification strategies, which will be elaborated in Section IV.

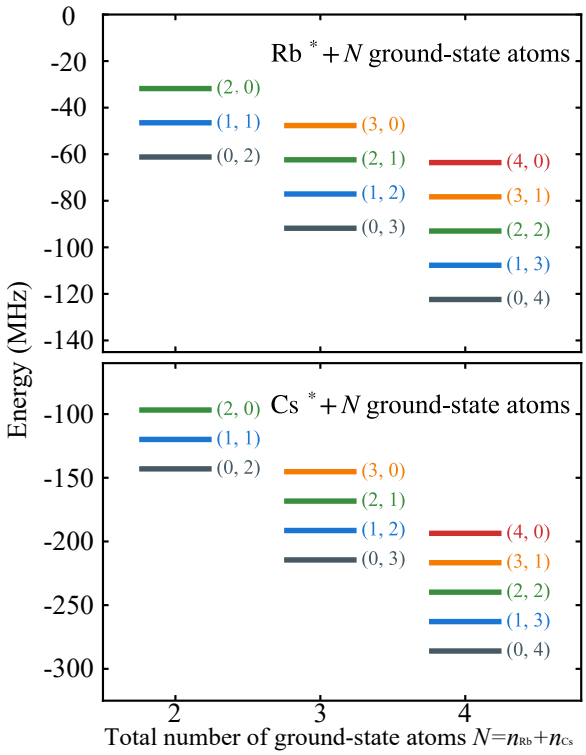


Figure 4. Binding energies of polyatomic ULRMs in Rb-Cs mixtures for the $37S_{1/2}$ state with $F = 1, 3$ and $\Omega = 0.5$. The top (bottom) panel shows molecules formed by an excited Rb^* (Cs^*) atom and N ground-state atoms. The binding energies are plotted as a function of the total number of ground-state atoms $N = n_{Rb} + n_{Cs}$. Each level corresponds to a specific atomic composition labeled by (n_{Rb}, n_{Cs}), indicating the numbers of ground-state Rb and Cs atoms, respectively. Color-coding denotes the number of ground-state Rb atoms to clearly distinguish the compositional dependence of the binding energy for a fixed total atom number N.

IV. DISCUSSION

A. Model Validity and Limitations

In this work, we focus on the vibrational spectra of diatomic heteronuclear ULRMs. However, we have not yet considered the effects of external electric fields, which are known to significantly influence the structure and stability of Rydberg molecules. Future investigations may incorporate such effects to explore field-induced dipole moments and possible alignment mechanisms. In addition, for Rydberg states with higher angular momentum, such as p, d, or even high-ℓ ($\ell > 2$) states, the anisotropic nature of their electronic wavefunctions can lead to energy shifts in polyatomic heteronuclear Rydberg molecules that are not simply integer multiples of the corresponding diatomic shifts. This nontrivial behavior presents another interesting direction for future research. Our calculations are based on the Fermi pseudopotential model, which approximates the short-range electron-atom interaction by a zero-range δ-function potential. While this approach allows for the inclusion of fine and hyperfine structure effects, it remains an approximate method. In particular, it suffers from a known limitation in the treatment of p-wave scattering, where the scattering volume diverges at specific values of the electron momentum k, leading to unphysical behavior in the potential energy curves. To overcome these issues, Greene *et al.* have developed a nonperturbative Green's function description of the electronic eigenstates in Rydberg-ground state diatomic molecules [43]. This method incorporates, in principle, all spin-dependent interactions in addition to the basic Coulombic Hamiltonian. It avoids the use of a pseudopotential altogether and naturally circumvents the divergences associated with p-wave shape resonances. Moreover, the approach is fully energy-consistent, enabling more accurate determination of potential energy curves and rovibrational spectra. Other theoretical efforts to compute have also been proposed, including two-electron R-matrix calculations [44] and generalized local frame-transformation theory [45]. However, these methods have yet to be extended to incorporate the complete set of spin-orbit and hyperfine interactions, and doing so remains a significant challenge.

B. Discrimination of Degenerate Polyatomic Molecular Configurations

For the formation of polyatomic molecules, it is sufficient that the atomic density is high enough for multiple ground-state atoms to be simultaneously located within the Rydberg electron orbit. Under resonant excitation conditions, polyatomic Rydberg molecules can then be formed [15]. As discussed in the previous section, although the binding energies of polyatomic heteronuclear molecules are theoretically discrete, the typical level spacing of approximately 1 MHz is difficult to resolve experimentally with current spectral linewidths. This limitation can be partially mitigated by controlling the atomic densities of Rb and Cs, which enables selective enhancement of signals associated with different molecular configurations.

As an illustrative example, the theoretical analysis shows that the Rb^*RbCs and Rb^*Rb_3 configurations are nearly degenerate (see Fig. 4). However, the formation of Rb^*Rb_3 requires four Rb atoms and, in the nonsaturated photoassociation regime, its signal strength is therefore expected to scale with the fourth power of the Rb atomic density [26]. In contrast, the Rb^*RbCs molecule consists of two Rb atoms and one Cs atom, and its signal strength scales quadratically with the Rb density and linearly with the Cs density. Based on these distinct scaling behaviors, three complementary experimental strategies can be employed to distinguish the near-degenerate configurations: (1) by comparing spectra obtained with and without trapping Cs atoms, since in the absence of Cs only Rb^*Rb_3 molecules can be formed; (2) by fixing the

Rb density and gradually increasing the Cs density, which leads to a corresponding enhancement of the Rb*RbCs signal; (3) by fixing the Cs density while varying the Rb density, where the Rb^*Rb_3 signal exhibits a quartic dependence on the Rb density, whereas the Rb*RbCs signal shows only a quadratic dependence.

Furthermore, upon ionization, Rb^*Rb_3 molecules predominantly decay into stable Rb^+ and Rb_2^+ ions, which appear as two distinct groups in the time-of-flight spectrum due to their different mass-to-charge ratios under electric-field acceleration [46]. In contrast, the ionization of Rb*RbCs molecules, in addition to producing Rb^+ and Rb_2^+ ions, may also lead to the formation of heteronuclear molecular $RbCs^+$, thereby providing at least three distinct features in the time-of-flight spectrum.

Finally, the application of an external electric field provides an additional means of discrimination. Since different molecular configurations possess different permanent electric dipole moments, their energy levels exhibit distinct shifts due to the Stark effect [2, 3]. This difference in Stark shifts can therefore be used as an independent method to distinguish between various molecular configurations.

SUMMARY

In summary, we have theoretically studied the formation and vibrational spectra of heteronuclear ULRMs in ultracold Rb and Cs gases. Our analysis focuses on both diatomic and polyatomic configurations involving $37S$ Rydberg states. To model these systems, we construct molecular Hamiltonian that incorporate s- and p-wave electron–atom scattering within the Fermi pseudopotential framework, including spin-orbit and hyperfine interactions of the ground-state atoms. By diagonalizing the resulting adiabatic Hamiltonian on a grid of internuclear distances, we obtain PECs for various molecular states. The vibrational bound states are computed by numerically solving the one-dimensional Schrödinger equation using these PECs. In particular, we focus on the vibrational ground-state levels supported by the outermost deep potential wells, which are expected to dominate the observed vibrational spectra. For polyatomic ULRMs, we predict binding energies based on additive combinations of dimer energies, analyze the degeneracy of vibrational levels, and discuss possible experimental schemes to lift these degeneracies. Our theoretical predictions may guide experimental efforts in probing heteronuclear ULRMs and support their applications in investigating the fundamental properties of Rydberg atoms and their interactions with ground-state atoms, while providing a benchmark for *ab initio* calculations.

ACKNOWLEDGMENTS

We acknowledge Matthew T. Eiles for providing the scattering phase shift data for Rb and Cs atoms, and for his valuable guidance on the computational methods. We also acknowledge Weibin Li for sharing his computational codes implementing the simplest version of the Fermi pseudopotential model for ULRMs, which includes only s-wave scattering and neglects both fine and hyperfine structure. This work was supported by the National Key R&D Program of China (Grant No. 2022YFA1404002), the National Natural Science Foundation of China (Grants No. T2495253, No. 61525504, and No. 61435011), and the Major Science and Technology Projects in Anhui Province (Grant No. 202203a13010001).

AUTHOR CONTRIBUTION

D-S. D. formulated the plan and provided support for this project. Q. L. performed the theoretical calculations and wrote the manuscript, and S-Y. S. provided many valuable insights. All authors participated in the discussions and provided valuable suggestions.

[1] C. H. Greene, A. Dickinson, and H. Sadeghpour, Creation of polar and nonpolar ultralong-range Rydberg molecules, Phys. Rev. Lett. **85**, 2458 (2000).
[2] V. Bendkowsky, B. Butscher, J. Nipper, J. P. Shaffer, R. Löw, and T. Pfau, Observation of ultralong-range Rydberg molecules, Nature **458**, 1005 (2009).
[3] W. Li, T. Pohl, J. Rost, S. T. Rittenhouse, H. R. Sadeghpour, J. Nipper, B. Butscher, J. Balewski, V. Bendkowsky, R. Löw, *et al.*, A homonuclear molecule with a permanent electric dipole moment, Science **334**, 1110 (2011).
[4] J. B. Balewski, A. T. Krupp, A. Gaj, D. Peter, H. P. Büchler, R. Löw, S. Hofferberth, and T. Pfau, Coupling a single electron to a bose–einstein condensate, Nature **502**, 664 (2013).
[5] D. Booth, S. Rittenhouse, J. Yang, H. Sadeghpour, and J. Shaffer, Production of trilobite Rydberg molecule dimers with kilo-Debye permanent electric dipole moments, Science **348**, 99 (2015).
[6] M. Althön, M. Exner, R. Blättner, and H. Ott, Exploring the vibrational series of pure trilobite Rydberg molecules, Nat. Commun. **14**, 8108 (2023).
[7] T. Niederprüm, O. Thomas, T. Eichert, C. Lippe, J. Pérez-Ríos, C. H. Greene, and H. Ott, Observation of pendular butterfly Rydberg molecules, Nat. Commun. **7**, 12820 (2016).
[8] A. T. Krupp, A. Gaj, J. B. Balewski, P. Ilzhöfer, S. Hofferberth, R. Löw, T. Pfau, M. Kurz, and P. Schmelcher, Alignment of D-state Rydberg molecules, Phys. Rev. Lett. **112**, 143008 (2014).

[9] F. Hummel, C. Fey, and P. Schmelcher, Alignment of s-state Rydberg molecules in magnetic fields, Phys. Rev. A **99**, 023401 (2019).

[10] S. T. Rittenhouse and H. Sadeghpour, Ultracold giant polyatomic Rydberg molecules: coherent control of molecular orientation, Phys. Rev. Lett. **104**, 243002 (2010).

[11] S. T. Rittenhouse, M. Mayle, P. Schmelcher, and H. Sadeghpour, Ultralong-range polyatomic Rydberg molecules formed by a polar perturber, J. Phys. B: At., Mol. Opt. Phys. **44**, 184005 (2011).

[12] R. González-Férez, H. Sadeghpour, and P. Schmelcher, Rotational hybridization, and control of alignment and orientation in triatomic ultralong-range Rydberg molecules, New J. Phys. **17**, 013021 (2015).

[13] R. González-Férez, S. T. Rittenhouse, P. Schmelcher, and H. Sadeghpour, A protocol to realize triatomic ultralong range Rydberg molecules in an ultracold krb gas, J. Phys. B: At., Mol. Opt. Phys. **53**, 074002 (2020).

[14] A. Guttridge, D. K. Ruttley, A. C. Baldock, R. González-Férez, H. Sadeghpour, C. Adams, and S. L. Cornish, Observation of Rydberg blockade due to the charge-dipole interaction between an atom and a polar molecule, Phy. Rev. Lett **131**, 013401 (2023).

[15] A. Gaj, A. T. Krupp, J. B. Balewski, R. Löw, S. Hofferberth, and T. Pfau, From molecular spectra to a density shift in dense Rydberg gases, Nat. Commun. **5**, 4546 (2014).

[16] C. Fey, J. Yang, S. T. Rittenhouse, F. Munkes, M. Baluktsian, P. Schmelcher, H. R. Sadeghpour, and J. P. Shaffer, Effective three-body interactions in $Cs(6s) - Cs(nd)$ Rydberg trimers, Phys. Rev. Lett. **122**, 103001 (2019).

[17] P. J. Luukko and J.-M. Rost, Polyatomic trilobite Rydberg molecules in a dense random gas, Phys. Rev. Lett. **119**, 203001 (2017).

[18] C. Fey, F. Hummel, and P. Schmelcher, Building principle of triatomic trilobite Rydberg molecules, Phys. Rev. A **99**, 022506 (2019).

[19] A. Junginger, J. Main, and G. Wunner, Quantum-classical lifetimes of Rydberg molecules, J. Phys. B: At., Mol. Opt. Phys. **46**, 085201 (2013).

[20] B. Butscher, V. Bendkowsky, J. Nipper, J. B. Balewski, L. Kukota, R. Löw, T. Pfau, W. Li, T. Pohl, and J. M. Rost, Lifetimes of ultralong-range Rydberg molecules in vibrational ground and excited states, J. Phys. B: At., Mol. Opt. Phys. **44**, 184004 (2011).

[21] F. Camargo, J. Whalen, R. Ding, H. Sadeghpour, S. Yoshida, J. Burgdörfer, F. Dunning, and T. Killian, Lifetimes of ultralong-range strontium Rydberg molecules, Phys. Rev. A **93**, 022702 (2016).

[22] J. Whalen, F. Camargo, R. Ding, T. Killian, F. Dunning, J. Pérez-Ríos, S. Yoshida, and J. Burgdörfer, Lifetimes of ultralong-range strontium Rydberg molecules in a dense bose-einstein condensate, Phys. Rev. A **96**, 042702 (2017).

[23] M. T. Eiles, Formation of long-range Rydberg molecules in two-component ultracold gases, Phys. Rev. A **98**, 042706 (2018).

[24] A. Wojciechowska, M. Tomza, and M. T. Eiles, Ultralong-range Rydberg molecules of Hg atoms, Phys. Rev. A **111**, 042816 (2025).

[25] J. Whalen, S. Kanungo, Y. Lu, S. Yoshida, J. Burgdörfer, F. Dunning, and T. Killian, Heteronuclear Rydberg molecules, Phys. Rev. A **101**, 060701 (2020).

[26] M. Peper and J. Deiglmayr, Heteronuclear long-range Rydberg molecules, Phys. Rev. Lett. **126**, 013001 (2021).

[27] A. Guttridge, T. R. Hepworth, D. K. Ruttley, A. A. Durst, M. T. Eiles, and S. L. Cornish, Individual assembly of two-species Rydberg molecules using optical tweezers, Phy. Rev. Lett **134**, 133401 (2025).

[28] J. Whalen, S. Kanungo, R. Ding, M. Wagner, R. Schmidt, H. Sadeghpour, S. Yoshida, J. Burgdörfer, F. Dunning, and T. Killian, Probing nonlocal spatial correlations in quantum gases with ultra-long-range Rydberg molecules, Phys. Rev. A **100**, 011402 (2019).

[29] S. Kanungo, Y. Lu, F. B. Dunning, S. Yoshida, J. Burgdörfer, and T. Killian, Measuring nonlocal three-body spatial correlations with Rydberg trimers in ultracold quantum gases, Phys. Rev. A **107**, 033322 (2023).

[30] P. Giannakeas, M. T. Eiles, F. Robicheaux, and J. M. Rost, Dressed ion-pair states of an ultralong-range Rydberg molecule, Phys. Rev. Lett. **125**, 123401 (2020).

[31] M. T. Eiles, Trilobites, butterflies, and other exotic specimens of long-range Rydberg molecules, J. Phys. B: At., Mol. Opt. Phys. **52**, 113001 (2019).

[32] E. Fermi, Sopra lo spostamento per pressione delle righe elevate delle serie spettrali, Nuovo Cim **11**, 157 (1934).

[33] A. Omont, On the theory of collisions of atoms in Rydberg states with neutral particles, J. De. Phys. **38**, 1343 (1977).

[34] E. L. Hamilton, C. H. Greene, and H. Sadeghpour, Shape-resonance-induced long-range molecular Rydberg states, J. Phys. B: At., Mol. Opt. Phys. **35**, L199 (2002).

[35] A. Khuskivadze, M. Chibisov, and I. Fabrikant, Adiabatic energy levels and electric dipole moments of Rydberg states of Rb_2 and Cs_2 dimers, Phys. Rev. A **66**, 042709 (2002).

[36] C. Bahrim, U. Thumm, and I. Fabrikant, ^3S_e and ^1S_e scattering lengths for e^-+ Rb, Cs and Fr collisions, J. Phys. B: At., Mol. Opt. Phys. **34**, L195 (2001).

[37] M. Exner, R. Srikumar, R. Blättner, M. T. Eiles, P. Schmelcher, and H. Ott, High precision spectroscopy of trilobite Rydberg molecules, Phys. Rev. Lett. **134**, 223401 (2025).

[38] M. T. Eiles and C. H. Greene, Hamiltonian for the inclusion of spin effects in long-range Rydberg molecules, Phys. Rev. A **95**, 042515 (2017).

[39] N. Šibalić, J. D. Pritchard, C. S. Adams, and K. J. Weatherill, Arc: An open-source library for calculating properties of alkali Rydberg atoms, Computer Physics Communications **220**, 319 (2017).

[40] J. J. Sakurai, S. Fu Tuan, and R. G. Newton, Modern quantum mechanics (1986).

[41] D. A. Anderson, S. A. Miller, and G. Raithel, Angular-momentum couplings in long-range rb 2 Rydberg molecules, Phys. Rev. A **90**, 062518 (2014).

[42] P. Goy, J. Raimond, G. Vitrant, and S. Haroche, Millimeter-wave spectroscopy in cesium Rydberg states. Quantum defects, fine-and hyperfine-structure measurements, Physical Review A **26**, 2733 (1982).

[43] C. H. Greene and M. T. Eiles, Green's-function treatment of Rydberg molecules with spins, Phys. Rev. A **108**, 042805 (2023).

[44] M. Tarana, Long-range Rydberg molecule Rb 2: Two-electron R-matrix calculations at intermediate internuclear distances, Phys. Rev. A **102**, 062802 (2020).

[45] P. Giannakeas, M. T. Eiles, F. Robicheaux, and J. M. Rost, Generalized local frame-transformation theory for

ultralong-range Rydberg molecules, Phys. Rev. A **102**, 033315 (2020).

[46] T. Niederprüm, O. Thomas, T. Manthey, T. M. Weber, and H. Ott, Giant cross section for molecular ion formation in ultracold Rydberg gases, Phy. Rev. Lett **115**, 013003 (2015).